[논 문] 한국재료학회지
Korean J. Mater. Res.
Vol. 32, No. 6 (2022)

https://doi.org/10.3740/MRSK.2022.32.6.287

Optimized Thermoelectric Properties in Zn-doped Zintl Phase Magnesium-Antimonide

Md. Mahmudur Rahman and Soon-Chul Ur†

Dept. of Material Sci. and Eng., Research Center for Sustainable Eco-Devices and Materials (ReSEM), Korea National University of Transportation, Chungju, Chungbuk, Republic of Korea

(Received April 13, 2022 : Revised May 30, 2022 : Accepted May 30, 2022)

Abstract Magnesium-antimonide is a well-known zintl phase thermoelectric material with low band gap energy, earth-abundance and characteristic electron-crystal phonon-glass properties. The nominal composition $Mg_{3.8-x}Zn_xSb_2$ ($0.00 \leq x \leq 0.02$) was synthesized by controlled melting and subsequent vacuum hot pressing method. To investigate phase development and surface morphology during the process, X-ray diffraction (XRD) and scanning electron microscopy (SEM) were carried out. It should be noted that an additional 16 at. % Mg must be added to the system to compensate for Mg loss during the melting process. This study evaluated the thermoelectric properties of the material in terms of Seebeck coefficient, electrical conductivity and thermal conductivity from the low to high temperature regime. The results demonstrated that substituting Zn at Mg sites increased electrical conductivity without significantly affecting the Seebeck coefficient. The maximal dimensionless figure of merit achieved was 0.30 for x = 0.01 at 855 K which is 30% greater than the intrinsic value. Electronic flow properties were also evaluated and discussed to explain the carrier transport mechanism involved in the thermoelectric properties of this alloy system.

Key words Zintl phase, Mg_3Sb_2, Zn doped, controlled melting, thermoelectric.

1. Introduction

Thermoelectric technology has experienced a great attention for its ability to convert waste heat into electricity and vice-verse.[1)] Thermoelectric generators are considerably sound pollution free because it doesn't have any moving parts, and comparatively more cost-effective. These advantages make thermoelectricity a potential candidate to help lessen the energy crisis existing in the world. The efficiency of a thermoelectric material is governed by the dimensionless figure of merit (ZT), which is expressed by following equation:

$$ZT = \frac{S^2\sigma}{\kappa}T \quad (1)$$

Here, S, σ, κ, and T are Seebeck coefficient, electrical conductivity, thermal conductivity, and temperature in kelvin respectively. In order to achieve high ZT value, large S and σ are required together with low κ. Various strategies were taken to obtain high ZT value either lowered the thermal conductivity by enhancing phonon scattering[2-3)] or increased the electronic properties by tuning the carrier concentration.[4-5)]

Zintl phase materials are considered as promising thermoelectric material due to low band gap energy, complex crystal structure, and semi-metal behavior. Typically, zintl compounds have two ionic sites where one is electropositive cation and other is electronegative anion.[6)] The electropositive cation can donate electron to the electronegative anion, ultimately makes the compound ionic in nature. Additionally, if cation accommodates insufficient number of electrons to donate anion, the valance shell of anion will remain incomplete. Therefore, anion bound to another anion by forming covalent bond. The existence of both ionic and covalent bond makes the structure of zintl compound more complex, providing characteristics electron-crystal phonon-glass properties.[7)] The complex crystal structure of a zintl compound can

†Corresponding author
E-Mail : scur@ut.ac.kr (S.-C. Ur, ReSEM)

provide a window for exact tuning of transport properties as well as can execute low thermal conductivity.

Zintl Mg_3Sb_2 consists of both cubic and hexagonal crystal structure.[7] The cubic crystal structure of this compound is known as α-Mg_3Sb_2, a high temperature phase comprises with 48 Mg and 32 Sb atoms, similar crystal structure of α-La_2O_3. However, hexagonal crystal structure of Mg_3Sb_2 is familiar as β-Mg_3Sb_2 which is a low temperature phase similar to crystal structure of Mn_2O_3. It contains two distinct Mg sites where ionic Mg^{2+} cation can donate electron to $[Mg_2Sb_2]^{2-}$ sites, resulting in typical behavior of a zintl compound.[8]

In particular, n-type Mg_3Sb_2 revealed high ZT values due to its high electronic and transport properties.[9-13] On the contrary, its p-type counterpart showed low ZT values due to the poor electrical properties, which strictly limited its practical application. Addressing this, numerous experiments were taken to improve the ZT value of p-type Mg_3Sb_2 but still it remains less than unity.

Several dopant elements were introduced in Mg_3Sb_2 system either by spark plasma sintering (SPS) or conventional hot press sintering process aiming to achieve high ZT value for p-type Mg_3Sb_2.[14-17] In this study, small amount of Zn was substituted at Mg sites in order to improve thermoelectric properties of p-type Mg_3Sb_2. Theoretical calculation has shown that Zn can act as an effective p-type dopant because the formation energy of Zn interstitials is fairly high compared to Mg interstitials.[18] The p-type $Mg_{3.8-x}Zn_xSb_2$ ($0.00 \leq x \leq 0.02$) have been synthesized via a solid-state reaction followed by controlled melting, pulverizing and vacuum hot pressing. This procedure is very innovative for this kind of alloy system and shortened the entire processing time.[19-20] A. Bhardwaj et al reported thermoelectric properties of Zn doped Mg_3Sb_2, synthesized by ball milling followed by SPS where carrier concentration was tuned.[8] In this study, vacuum hot pressing is used as consolidation process where the applied pressure can increase the rate of densification at given temperature.[21] This can produce final product with small grain size due to independent behavior of grain growth under pressure. Though vacuum hot pressing is less effective technique in terms of density measurement compared to SPS process, the density for all of end product in this study is shown to be very close to theoretical density.[19]

Initially, single phase magnesium antimonide is confirmed by adding excessive amount of Mg because nominal composition of this compound is usually evolved with excessive Sb.[19] This might be happened due to the evaporation of Mg during the melting process.[11-12] This study demonstrated that substitution of Zn in the solid solution $Mg_{3.8-x}Zn_xSb_2$ improved electronic properties as well as lowered the thermal conductivity, resulted higher ZT value compared to pristine one. The obtained ZT value is highly comparable to other study.

2. Experimental Procedure

Nominal compositions of $Mg_{3.8-x}Zn_xSb_2$ ($0.00 \leq x \leq 0.02$) were synthesized by using the elemental shots of Mg (99.9 % purity, Kojundo), Sb (99.999 % purity, Kojundo) and Zn (99.9 % purity, Kojundo). Sample was measured by a weight balance and put into a graphite crucible. The graphite crucible with a stopper was taken and its inner walls were coated by a wide layer of boron-nitrate (BN) in order to confirm controlled melting. Graphite crucible was then put into the vacuum furnace and heated at 1173 K for 1 hour. After the melting and cooling process, a mortar pestle was taken to pulverize the cooled ingot. After pulverizing, fine particles were collected by sieving under 325 meshes. The entire process was done under Ar gas atmosphere. Then, vacuum hot pressing (VHP) was considered in order to consolidate the sample at 70 MPa and 873 K for 4 hours. In order to confirm the phases, X-ray diffraction (XRD, BRUKER AXS Advance D-8, Germany) with Cu-Kα radiation source was carried out. Scanning electron microscopy (SEM, Quanta-400, Netharland) was taken to investigate the surface morphology. The samples were made in a cylindrical shape ($3 \times 3 \times 10$ mm^3) in order to measure the Seebeck coefficient as well as electrical conductivity by performing with ZEM-3 (ULVAC-RIKO, Japan). Thermal diffusivity (d) was achieved by laser flash method of TC-9000H (ULVAC-RIKO, Japan). According to Archimedes principle, density (r) of all prepared sample were measured to calculate thermal conductivity (k) via an equation, $k = d \times C_P \times r$. Here, C_P was specific heat capacity of Mg_3Sb_2 which was taken from literature.[22] Transport properties were evaluated by Van der Pauw method (modified keithley-7065, USA) at a constant magnetic field (1T) and constant electric current (50 mA).

3. Result and Discussion

Fig. 1(a) represents X-ray diffraction (XRD) characterization for VHPed $Mg_{3.8-x}Zn_xSb_2$. As a reference, XRD diffraction for $x = 0.005$ after melting is plotted in the figure. As it can be seen, a trace amount of ZnSb was formed during the process for both casted and VHPed $x = 0.005$. This is possibly due to the evaporation of Mg throughout the process, which is consistent with other studies.[10] Besides this, no other secondary phases were observed. Fig. 1(b) outlines lattice parameters a, c for VHPed $Mg_{3.8-x}Zn_xSb_2$ as a function of Zn concentration (x). Lattice parameters are seen to increase with increasing x. Since Zn has larger ionic radii (0.74 Å) than that of Mg (0.66 Å),

substitution of Zn at Mg sites may increase the lattice parameter, and lower the diffraction angle as shown in Fig. 1(c).[20,23] This might indicate that Zn was successfully doped through Mg_3Sb_2 system.

The microstructure of pulverized powders for $Mg_{3.79}Zn_{0.01}Sb_2$ is shown in Fig. 2(a). Since samples were sieved through 325 meshes after pulverization, the particles were typically angular in shape and less than 45 μm in diameter. Fig. 2(b) outlines the surface morphology of the fractured sample for VHPed $Mg_{3.79}Zn_{0.01}Sb_2$. As it can be seen, sample shows dense microstructure without any obvious internal flaws. This is agreeable with the

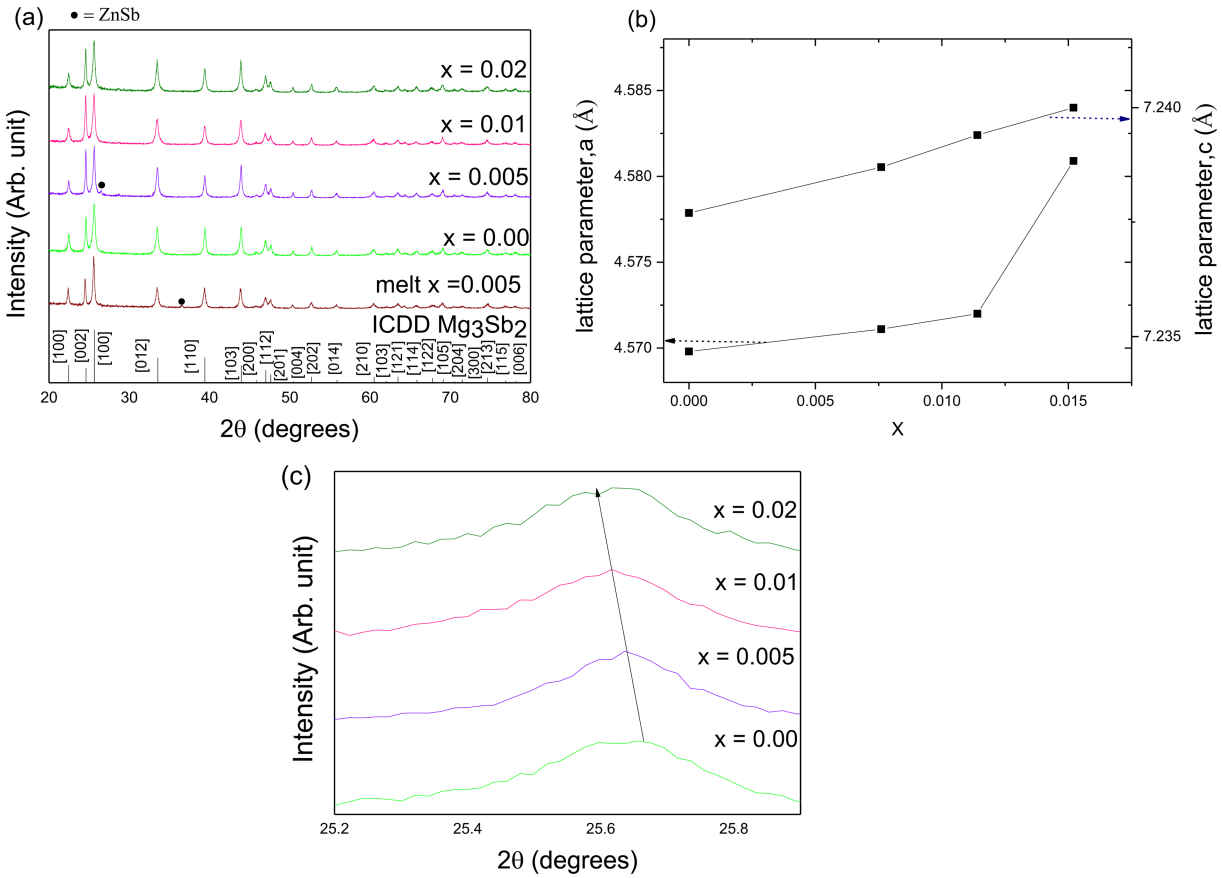

Fig. 1. XRD diffraction pattern of $Mg_{3.8-x}Zn_xSb_2$ for (a) VHPed sample and (b) lattice parameter with respect to Zn content (x), and (c) the peak shift for (100) line.

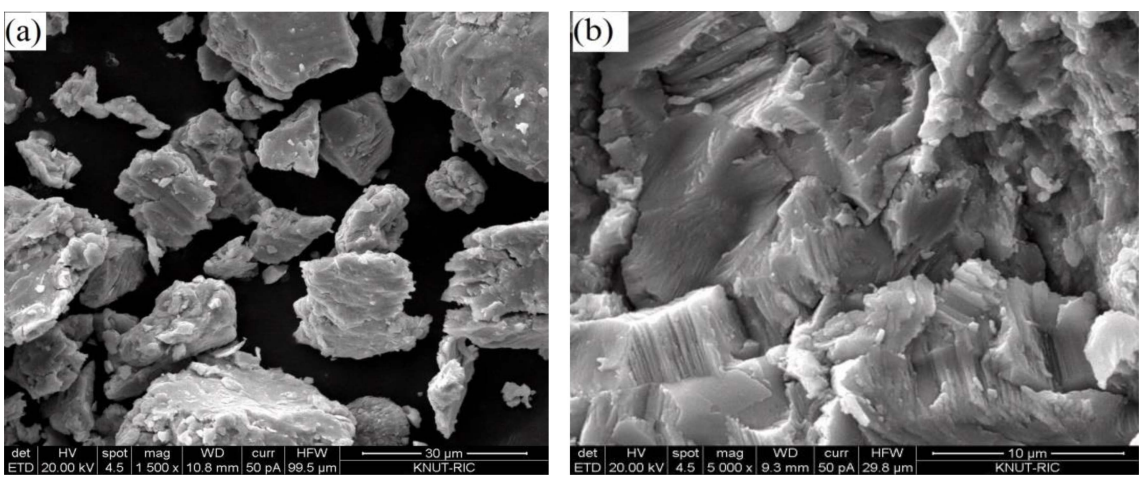

Fig. 2. Scanning electron microscopy of (a) as-sieved and (b) fractured surface of VHPed $Mg_{3.79}Zn_{0.01}Sb_2$.

density measurement as shown in Table 2. The characteristics of lamellar structure is typically observed in this material system as in other studies.[24] Energy dispersive X-ray spectroscopy (EDS) mapping with a line profile for VHPed $Mg_{3.79}Zn_{0.01}Sb_2$ is displayed in Fig. 3. It can be seen that Mg, Sb and Zn are homogenously distributed around the detected area without any obvious impurities. As shown in Fig. 3, EDS line profile shows that Zn is uniformly distributed throughout the samples, indicating that doping has done successfully. The compositional analysis of the fractured sample for VHPed $Mg_{3.8-x}Zn_xSb_2$ was done by employing SEM-EDS as shown in Table 1. Though slight discrepancy in the nominal and final compositions in EDS analysis is shown, which could be from sampling error and detection limit of EDS, the compositional observation seems to be matched together in general.

Fig. 4(a) outlines the temperature dependence of electrical conductivity σ(T) for the synthesized pellets. As it can be seen, the electrical conductivity is increased with increasing temperature, corresponding to intrinsic semiconductor behavior. At room temperature, all compositions display high electrical resistivity. Nevertheless, beyond 473 K, these semiconductors exhibit an increase in electrical conductivity. This may suggest that majority carriers (holes) can achieve sufficient energy to overcome

Table 1. Composition of the VHPed samples observed in EDS analysis.

Nominal composition $Mg_{3.8-x}Zn_xSb_2$	Mg (at. %)	Sb (at. %)	Zn (at. %)
x = 0.00	55.91	44.09	0.00
x = 0.005	56.72	42.47	0.81
x = 0.01	54.15	45.69	0.15
x = 0.02	52.48	46.44	1.07

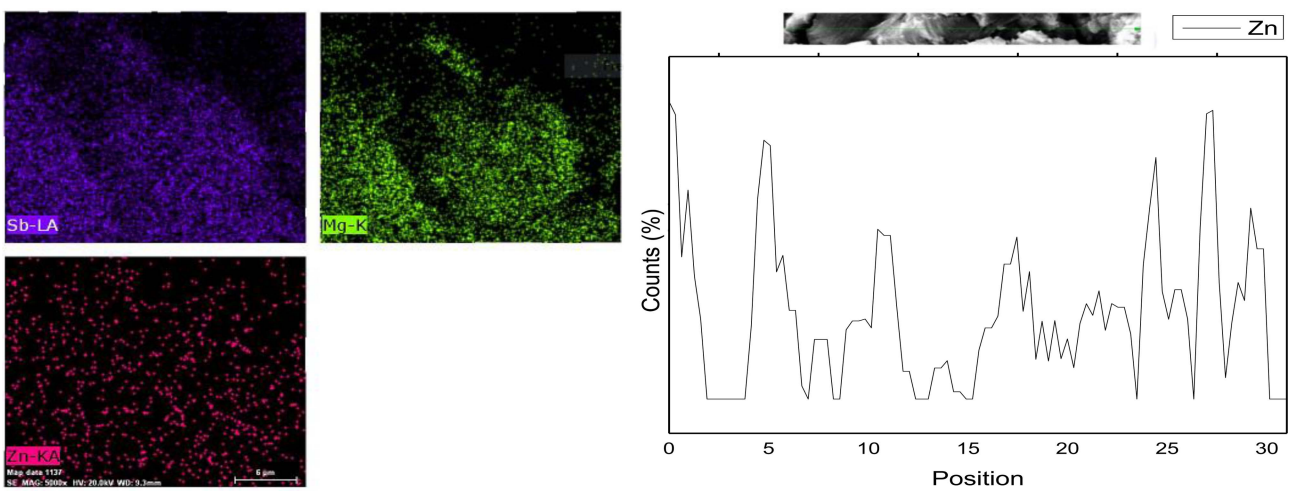

Fig. 3. EDS mapping for x = 0.01 shows elemental distribution of Mg, Sb and Zn and EDS line profile shows that of Zn for x = 0.01.

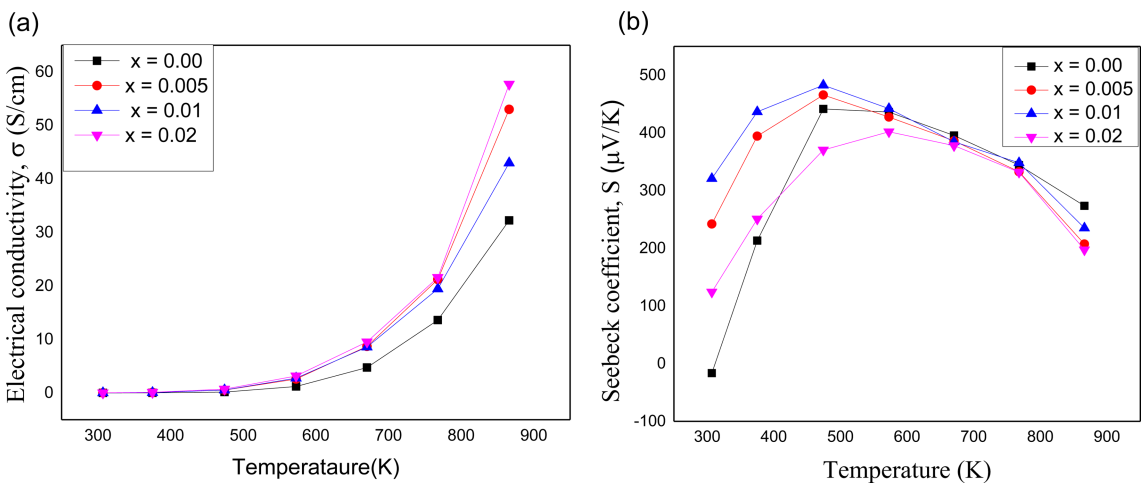

Fig. 4. Temperature dependence (a) electrical conductivity, (b) Seebeck coefficient of $Mg_{3.8-x}Zn_xSb_2$.

the energy barrier at 473 K. It is also observed that maximum σ for Zn content samples are higher than that of intrinsic one, possibly due to increase in carrier concentrations.

The change of Seebeeck coefficient (S) with respect to temperature and x is shown in Fig. 4(b). The positive value of S indicates that these are p-type semiconductors. However, a negative value of S is observed at room temperature for x = 0.00 presumably due to the presence of excess Mg, which is reported earlier in the previous study.[19] Initially, the Seebeck coefficient is seen to increase with temperature up to 473 K, after which it decreases with increasing temperature. As expected, the Seebeck coefficient variation behavior and electrical conductivity in the test temperature range seemed to fit well together. The majority carrier (holes) might be increased with increasing temperature, ultimately increased in electrical conductivity and lowered the Seebeck coefficient.[25]

The temperature dependence of total thermal conductivity (κ) and lattice thermal conductivity (κ_L) for $Mg_{3.8-x}Zn_xSb_2$ ($0.00 \leq x \leq 0.02$) are shown in Fig. 5(a) and 5(b) respectively. The result of total thermal conductivity can be explained by two components of κ, lattice thermal conductivity (κ_L) and electronic thermal conductivity (κ_E). Furthermore, from Widemann-Franz law, electronic thermal conductivity can be expressed via $\kappa_E = L\sigma T$ (the Lorenz number $L = 2.38\times10^{-8}$ $W\Omega K^{-2}$). The total thermal conductivity decreases with increasing Zn content x when $x \leq 0.01$ and then increases but it's still lower than that of intrinsic one. As shown in Fig. 5(a) and 5(b), the difference between κ and κ_L is very little which explain the main contributor of κ is κ_L. Substitution of Zn at Mg sites may introduce the point defect scattering due to large mass difference of Zn and Mg, which ultimately reduces lattice thermal conductivity.[26] It is also observed that total thermal conductivity is turned to elevate at 855 K for all composition. This is possibly due to increase in electrical conductivity at that temperature. The lowest thermal conductivity is achieved for x = 0.01 at 855 K,

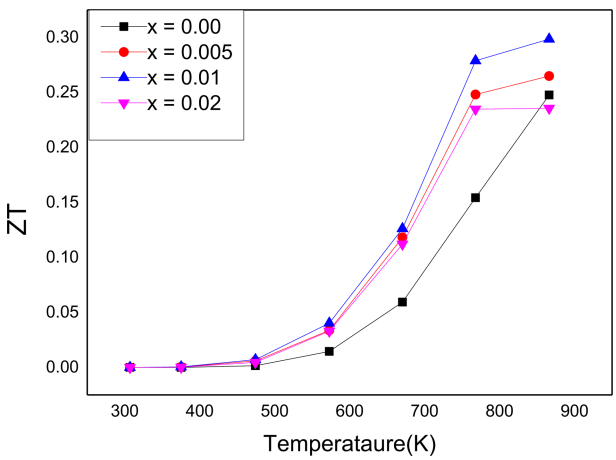

Fig. 6. Temperature dependence dimensionless figure of merit (ZT) of VHPed $Mg_{3.8-x}Zn_xSb_2$.

Table 2. Relative density and transport properties of vacuum hot pressed $Mg_{3.8-x}Zn_xSb_2$ samples at room temperature.

Nominal composition $Mg_{3.8-x}Zn_xSb_2$	Hall coefficient (cm^3C^{-1})	Carrier mobility ($cm^2V^{-1}S^{-1}$)	Carrier concentration ($\times10^{16}cm^{-3}$)	Relative density
x = 0.00	-155.82	0.265	-4.391	~ 99.10 %
x = 0.005	28.255	0.400	21.118	~ 99.16 %
x = 0.01	30.778	0.320	20.071	~ 99.19 %
x = 0.02	33.004	0.882	22.759	~ 99.23 %

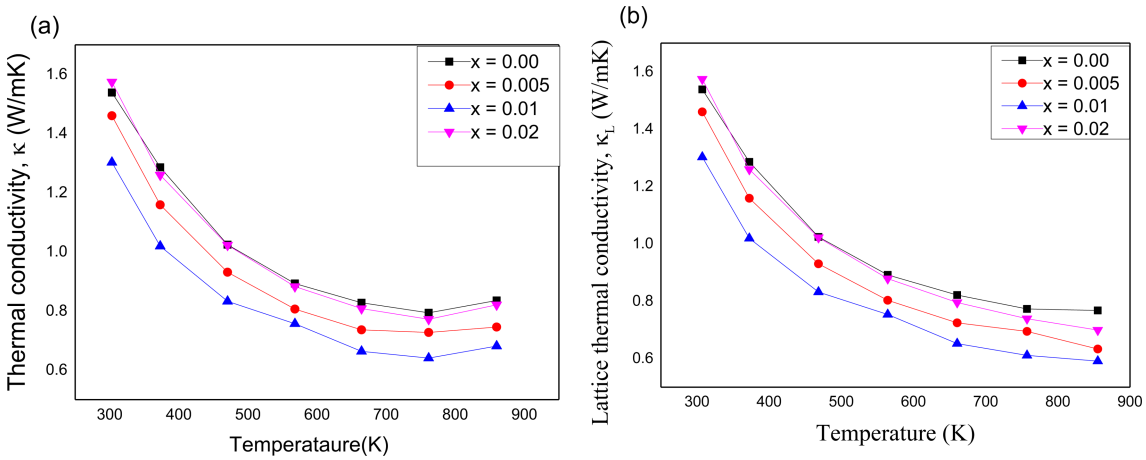

Fig. 5. Temperature dependence of (a) thermal conductivity and (b) lattice thermal conductivity of VHPed $Mg_{3.8-x}Zn_xSb_2$.

which is 18 % lower than that of intrinsic one. The reduction in thermal conductivity might be attributed to doping effect.

The dimensionless figure of merit (ZT) with respect to temperature and x is shown in Fig. 6. Sample $Mg_{3.79}Zn_{0.01}Sb_2$ exhibits a peak ZT ≈ 0.30 at 855 K due to its relatively lower thermal conductivity and best electronic properties. This improvement of ZT is 1.25 times higher than that of intrinsic one. The resultant ZT is also highly comparable to other study, regardless significantly low carrier concentration is observed in this study.

4. Conclusion

Nominal compositions of $Mg_{3.8-x}Zn_xSb_2$ ($0.00 \leq x \leq 0.02$) were successfully fabricated by the controlled melting and subsequent vacuum hot pressing method. Zn appeared to be uniformly distributed within the matrix and played a vital role as a dopant. The substitution of Zn at Mg sites has governed to tune the carrier concentration as well as carrier mobility, leading to rise in electrical conductivity without markedly lowering the Seebeck coefficient. Moreover, substitution of Zn in the solid solution $Mg_{3.8-x}Zn_xSb_2$ has managed to enhance phonon scattering, which is responsible to reduce the thermal conductivity. The systematic measurement shows the peak ZT value of 0.30 at 855 K, which is highly comparable to other studies. Further development can be made by tuning the carrier concentration either co-doping or composite fabrication method.

Acknowledgement

This research was supported by the Korea Basic Science Institute grant funded by the Ministry of Education (grant no. 2019R1A6C1010047).

References

1. A. R. M. Siddique, S. Mahmud and B. Van Heyst, Renew. Sustain. Energ. Rev., **73**, 730 (2017).
2. H. S. Dow, M. Na, S. J. Kim and J. W. Lee, J. Mater. Chem. C, **7**, 3787 (2019).
3. G. Joshi, H. Lee, Y. Lan, X. Wang, G. Zhu, D. Wang, R. W. Gould, D. C. Cuff, M. Y. Tang, M. S. Dresselhaus, G. Chen and Z. Ren, Nano Lett., **8**, 4670 (2008).
4. Y. Pei, Z. M. Gibbs, A. Gloskovskii, B. Balke, W. G. Zeier and G. J. Snyder, Adv. Energy Mater., **4**, 1400486 (2014).
5. Y. Zhao, J. S. Dyck, B. M. Hernandez and C. Burda, J. Am. Chem. Soc., **132**, 4982 (2010).
6. S. M. Kauzlarich, S. R. Brown and G. J. Snyder, J. Chem. Soc. Dalt. Trans., **21**, 2099 (2007).
7. A. Bhardwaj, A. Rajput, A. K. Shukla, J. J. Pulikkotil, A. K. Srivastava, A. Dhar, G. Gupta, S. Auluck, D. K. Misra and R. C. Budhani, RSC Adv., **3**, 8504 (2013).
8. A. Bhardwaj, N. S. Chauhan, S. Goel, V. Singh, J. J. Pulikkotil, T. D. Senguttuvan and D. K. Misra, Phys. Chem. Chem. Phys., **18**, 6191 (2016).
9. J. Zhang, L. Song, K. A. Borup, M. R. V. Jørgensen and B. B. Iversen, Adv. Energy Mater., **8**, 1 (2018).
10. H. Tamaki, H. K. Sato and T. Kanno, Adv. Mater., **28**, 10182 (2016).
11. J. Zhang, L. Song and B. B. Iversen, Angew. Chemie., **132**, 4308 (2020).
12. Y. Wang, X. Zhang, Y. Wang, H. Liu and J. Zhang, Phys. Status Solidi A, **216**, 1 (2019).
13. F. Zhang, C. Chen, H. Yao, F. Bai, L. Yin, X. Li, S. Li, W. Xue, Y. Wang, F. Cao, X. Liu, J. Sui and Q. Zhang, Adv. Funct. Mater., **30**, 1 (2020).
14. A. Bhardwaj and D. K. Misra, RSC Adv., **4**, 34552 (2014).
15. I.-K. Kim, K.-W. Jang and I.-H. Kim. Korean J. Mater. Res., **23**, 98 (2013).
16. A. Bhardwaj, N. S. Chauhan and D. K. Misra, J. Mater. Chem. A, **3**, 10777 (2015).
17. Z. Ren, J. Shuai, J. Mao, Q. Zhu, S. Song, Y. Ni and S. Chen, Acta Mater., **143**, 265 (2018).
18. P. Gorai, B. R. Ortiz, E. S. Toberer and V. Stevanović, J. Mater. Chem. A, **6**, 13806 (2018).
19. M. M. Rahman, A. K. M. A. Shawon and S.-C. Ur, Electron. Mater. Lett., **17**, 102 (2021).
20. A. K. M. A. Shawon, M. M. Rahman and S.-C Ur, Electron. Mater. Lett., **16**, 540 (2020).
21. J. Zhang, H. Zhang, J. Wu and J. Zhang, Pem Fuel Cell Testing and Diagnosis, p. 43–80, Elsevier (2013).
22. M. T. Agne, K. Imasato, S. Anand, K. Lee, S. K. Bux, A. Zevalkink, A. J. E. Rettie, D. Y. Chung, M. G. Kanatzidis and G. J. Snyder, Mater. Today Phys., **6**, 83 (2018).
23. A. Bhardwaj, N. S. Chauhan, S. Goel, V. Singh, J. J. Pulikkotil, T. D. Senguttuvan and D. K. Misra, Phys. Chem. Chem. Phys., **18**, 6191 (2016).
24. Y. Cui, X. Zhang, B. Duan, J. Li, H. Yang, H. Wang, P. Wen, T. Gao, Z. Fang, G. Li, Y. Li and P. Zhai, Mater. Electron., **30**, 15206 (2019).
25. H. Wang, J. Chen, T. Lu, K. Zhu, S. Li, J. Liu and H. Zhao, Chin. Phys. B, **27**, 1 (2018).
26. Q. G. Cao, H. Zhang, M. B. Tang, H. H. Chen, X. X. Yang, Y. Grin and J. T. Zhao, J. Appl. Phys., **107**, 10 (2010).

Author Information

Md. Mahmudur Rahman
한국교통대학교 석사과정 학생

Soon-Chul Ur
한국교통대학교 교수